

Metal-organic frameworks-derived titanium dioxide–carbon nanocomposite for supercapacitor applications

Vishal Shrivastav^{1,3} | Shashank Sundriyal^{2,4} | Ki-Hyun Kim⁵ |
Ravindra K. Sinha¹ | Umesh K. Tiwari^{1,3}  | Akash Deep^{2,3}

¹Advanced Materials and Sensors, CSIR-Central Scientific Instrument Organisation (CSIR-CSIO), Chandigarh, India

²Analytical Techniques, CSIR-Central Scientific Instrument Organisation (CSIR-CSIO), Chandigarh, India

³Academy of Scientific and Innovative Research (AcSIR-CSIO), Chandigarh, India

⁴Advanced Carbon Products and Metrology, CSIR-National Physical Laboratory (CSIR-NPL), New Delhi, India

⁵Department of Civil and Environmental Engineering, Hanyang University, Seongdong-gu, South Korea

Correspondence

Umesh K. Tiwari and Akash Deep, Academy of Scientific and Innovative Research (AcSIR-CSIO), Chandigarh 160030, India.

Email: umeshtiwari@csio.res.in (U. K. T.) and dr.akashdeep@csio.res.in (A. D.).

Funding information

Cooperative Research Program for Agriculture Science & Technology Development, Grant/Award Number: PJ014297; CSIR India project, Grant/Award Numbers: MLP-023, MLP-0029; Ministry of Environment, Grant/Award Number: 2018001850001; Ministry of Science and ICT, South Korea, Grant/Award Number: 2016R1E1A1A01940995

Summary

The pyrolysis of metal-organic frameworks (MOFs) to derive porous nanocarbons and metal oxides has attracted scientific attention due to the advantageous properties of the final products (eg, high surface areas). In the present research, MIL-125 (MIL = Materials of Institute Lavoisier, a Ti-based MOF) has been subjected to a single-step pyrolysis treatment in argon atmosphere. The combination of uniformly linked titanium metal cluster and oxygen-enriched organic linker has acted as a template to yield a titanium dioxide (TiO₂)–carbon nanocomposite. The TiO₂ nanoparticles infused in carbon skeleton structure (TiO₂/C) has been investigated as an electrode material for supercapacitor applications. TiO₂/C electrodes have delivered an excellent electrochemical performance, for example, in terms of charging–discharging efficiency. Two equally weighed TiO₂/C electrodes have been used to assemble a solid-state symmetrical supercapacitor (SC) device, containing a gel electrolyte (poly vinyl alcohol in 1 M H₂SO₄). The above device has delivered a high value of energy density (43.5 Wh/kg) and an excellent power output of 0.865 kW/kg. The symmetrical SC could retain almost 95% of its initial capacitance even after 2000 charging–discharging cycles. The electrochemical performance of the TiO₂/C SC was better than most MOF-based SCs reported previously. Such performance is attributed to the synergistic combination of electrically conducting MOF-derived carbon and redox active TiO₂ nanocrystals with a large specific surface area.

KEYWORDS

energy density, solid electrolyte, symmetric supercapacitor, synergy, TiO₂ infused carbon

1 | INTRODUCTION

In light of the growing demand for efficient energy storage devices, supercapacitors (SCs) have assumed a

paramount role.¹ SCs can yield about ten times greater power density than lithium-ion batteries, because of which they are envisaged as better options in many application areas including electric charge and discharge devices. They are projected as lightweight and flexible energy storage devices.^{2,3} SCs also assume great significance as alternative energy storage devices in relation to the harvesting of

Vishal Shrivastav and Shashank Sundriyal contributed equally to this study.

energy from solar and wind sources.^{4,5} They are considered to provide advantages over batteries with respect to fast charging/discharging rates and prolonged cycle life.⁶ Efforts are hence underway to develop SCs with high energy densities and appropriate cyclic stabilities to enhance their commercial viability.⁷

SCs work on the principles of both non-Faradaic (electric double-layer capacitor [EDLC]) and Faradaic (pseudocapacitance) charge storage mechanisms. In context of developing efficient electrode materials for SCs, it is important to control the surface morphology and the effective pore size distribution so as to ensure maximum surface area. Traditionally, metal oxides and carbon-based materials have been chosen for the fabrication of SC electrodes.⁸ For instance, in literature, TiO₂ has been widely reported because of its abundance, low cost, and limited volume change during the charging–discharging process.⁹ Nonetheless, the electronic conductivity of TiO₂ is generally low ($>10^{-12}$ S cm⁻¹), which restricts device performance to an extent. In comparison, the formation of composites of metal oxides with other conductive materials can facilitate relatively fast electronic transfer due to redox reaction. It can aid in the attainment of high-power outputs and dense charge storage capability. To date, TiO₂ has hence been mixed with various conductive agents (like metals, graphene, CNTs, and conducting polymers).¹⁰ However, most of the methods employed to synthesize the above composites involve cumbersome steps. Moreover, the impregnation of metal oxides nanoparticles inside the porous structure of conductive materials is not easily possible through the conventional synthesis routes. For example, researchers have attempted to synthesize a composite of TiO₂ with reduced graphene oxide (rGO). However, the complex synthesis steps and a poor distribution of TiO₂ nanoparticles in the host structure are a common stumbling block to researchers.^{8,11} The use of rGO sheets as a conductive material alongside the TiO₂ nanoparticles also faces the problem in terms of sheet agglomeration. Alternatively, TiO₂ nanoparticles can be distributed in porous carbon matrix with high uniformity and controlled crystallite size. Recently, Pant and coworkers have proposed the synthesis of TiO₂ nanoparticles distributed in carbon nanofibers through electrospinning process.¹² The above composite was then used in a SC with a specific capacitance (C_s) of 106.57 F/g (at current density of 1 A/g). Nonetheless, the electrospinning synthesis method involves various optimization parameters. Also, the nonuniform pore size distribution of the material with this method is another critical issue which cannot be ignored.¹³ In another report, Elmouwahidi et al demonstrated the use of TiO₂ nanoparticles-doped carbon xerogels for SC application.¹⁴ The sample delivered a C_s value of 137 F/g at a current density of 0.25 A/g. Nonetheless, it was not satisfactory as per the requirement of high-performance

energy storage SCs. The inverse emulsion method used to synthesize the composite in the above study did not necessarily yield the uniform carbon xerogels as microscopic images also showed irregularly shaped product. As the available information suggests, the synthesis of uniformly distributed TiO₂ nanoparticles in porous carbon matrix is not an easy task. There is a need to explore a new synthesis route that can be allowed to yield TiO₂/C composites with enhanced electrochemical performance. It should also be highlighted here that the electrochemical properties of TiO₂/C composites with respect to the structural phase (rutile or anatase) of the TiO₂ have scantily been studied in the literature.¹⁵

Metal-organic framework (MOF) is a new class of material with a metal cluster at the center connected with an organic linker. MOFs are characterized with tunable pore size distribution and hierarchical porous structure. However, their low conductivity limits the electronic pathways within the material and the redox behavior of the metal cluster is also hindered as they are coordinated with the organic linker. Lately, the pyrolysis of MOFs has been reported as an effective option to yield different types of metal oxides and nanoporous carbons.¹⁶ Generally, the MOF-derived metal oxides only show limited electrical conductivity. Moreover, the irreversible redox reaction and dissolution of metal oxide in the electrolyte is another major drawback to restrict their usage as an electrode material. MOF derived nanoporous carbon is a high specific surface area material and possesses a wide range of pore size distribution. These features have prompted the researchers to use MOF derived nano carbon in energy storage devices. Recently, ZIF-8 (zeolitic imidazolate framework-8) has been used to derive nanoporous carbon (surface area of 1523 m²/g), which was then proposed as a SC electrode material with a C_s value of 251 F/g (electrolyte = 1 M H₂SO₄).¹⁷ The charge storage mechanism in the above system was associated with the EDLC process.

MOF-derived metal oxides or nanoporous carbons, as individual electrode materials, have been reported with some exciting potential in SC applications. However, the composites of metal oxides and nanoporous carbons should offer clear merits over the individual materials. Such nanocomposites may facilitate the combination of the redox and EDLC mechanisms to uplift the electrochemical performance. Some MOFs can also offer possibilities to derive metal-oxide/nanocarbon composite via simple pyrolysis treatments.¹⁸

Recently, a Zn-Ti-MOF was processed with an oxidative desulfurization approach to obtain a TiO₂/C composite.¹⁹ The above nanocomposite was claimed as a highly mesoporous structure with well-dispersed TiO₂ nanoparticles in the carbon matrix. It was also projected for an excellent

catalytic performance. Another MOF, that is, MIL-125 (Ti) (MIL = Materials of Institute Lavoisier) has also been converted into TiO_2/C composite. The potential of this composite as an anode material for the lithium-ion batteries was found to have a high capacity of 400 mAh/g.²⁰ A similar composite was also proposed for sodium-ion battery application.²¹

As the available literature reveals, MOFs can be used as novel precursors to obtain metal oxide impregnated nanocarbon matrices. Such nanocomposites can be used to develop electrodes that can show stability against multiple charging/discharging cycles overcoming the issue of dissolution of the metal oxide nanoparticles in the electrolyte. To the best of our knowledge, MOF-derived TiO_2/C composite has not been investigated as an electrode material of aqueous electrolyte-based SCs. The influence of the different phases of TiO_2 in carbon matrix, vis-à-vis the electrochemical performance, is also an interesting matter of investigation.

By following a simple synthesis route, we report the pyrolytic conversion (1000°C) of MIL-125 (Ti) into a metal oxide/nanoporous carbon (TiO_2/C) hybrid material. As a main advantageous feature of the process, a single precursor was used to obtain the functional TiO_2/C hybrid. This process did not require any additional source of carbon. The synthesized TiO_2/C composite, when tested for its potential SC electrode application, offered a high specific capacitance value with remarkable cyclic stability. A series of combinations of two symmetrical TiO_2/C SCs was found capable of lighting up a white LED for about 4 minutes after a quick charge of only 40 seconds.

2 | RESULTS AND DISCUSSION

The synthesis and the other experimental procedures have been detailed in the Supporting information

A summary of the experimental scheme adopted for the synthesis of MIL-125 (Ti)-derived TiO_2/C composite is provided in Figure 1. MIL-125 (Ti) was synthesized via solvothermal route, followed by its pyrolysis to obtain TiO_2/C composite. The effect on pyrolysis temperature (600°C, 800°C, and 1000°C) has been correlated with the specific surface area and the meso-micropores distribution. The final product had a blackish appearance because of high-temperature pyrolysis treatment.

2.1 | XRD and thermal investigations

X-ray Diffraction (XRD) pattern of synthesized MOF matched well with literature confirming the successful formation of MOF (Figure S1).^{22,23} A characteristic 2θ peak around 6.9° was an important indicator to verify a successful synthesis of the MOF.²⁴ Also, the sharpness and the high-intensity peaks suggested the product of a high crystallinity in nature. Further to investigate the transformation of MIL-125 to TiO_2 nanoparticles-infused carbon composite with temperature, Thermogravimetric analysis (TGA) was performed up to 900°C (Figure S2). The initial weight loss of about 34% up to 170°C was attributed to the removal of the adsorbed gases and the evaporation of the solvent/adsorbed water molecules from the MOF pores. Second weight loss regime (21%) up to around 300°C was

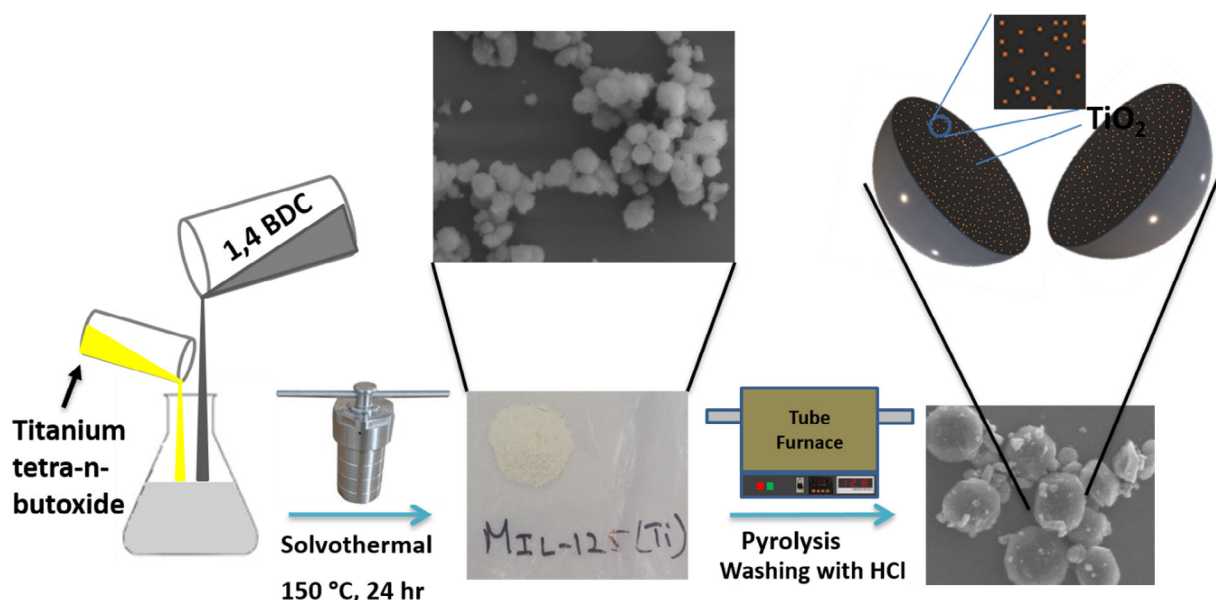


FIGURE 1 Schematic illustration of the synthesis of MIL-125 derived TiO_2/C composite nanostructures [Colour figure can be viewed at wileyonlinelibrary.com]

associated with the structural reorganization after the departure of hydroxyl groups bonded in between two titanium atoms.²³ Further weight loss of around 16.5% till 550°C indicated the collapse of the MIL-125 (Ti) structure (ie, breaking of Ti - linker bonds) and a subsequent formation of TiO₂-infused carbon composite. TGA data implied that the desired TiO₂/C composite could be obtained at 550°C or greater temperatures. Once converted, the material again displayed no significant weight loss up to 900°C, demonstrating the structural stability of TiO₂/C composite.

XRD patterns of the TiO₂/C composites obtained at different temperatures are presented in Figure 2A. A diffraction peak at 25.2° in TiO₂/C-600 sample can be indexed to (101) plane of the polycrystalline anatase phase of TiO₂²⁵ (JCPDS card 21-1272). A preferred formation of the anatase phase at a lower pyrolysis temperature can be explained on the structural basis. The formed unit cell

(TiO₆ octahedra) of anatase phase is long range ordered as compared to the unit cell of the rutile phase {Hearne, 2004 #203}. Because of this, anatase phase of TiO₂ faces low molecular restriction during nucleation process. This reason initiates the formation of anatase phase at lower temperature than rutile phase of TiO₂.²⁶ Alternatively, from the thermodynamics point of view, the anatase formation at lower temperature can also be explained with change in Gibbs free energy of the material. Such change reflects the combination of change in surface-free energy and the volume-free energy. The change in surface free energy is positive in nature that is, the material needs to extract the energy from the surrounding to form the surface (at the nucleation level). Whereas, the volume free energy of the materials are opposite to surface free energy.²⁷ Instead of extracting the energy, it releases the energy to the surrounding. However, during nucleation, the first thing is the formation of the surface subsequent

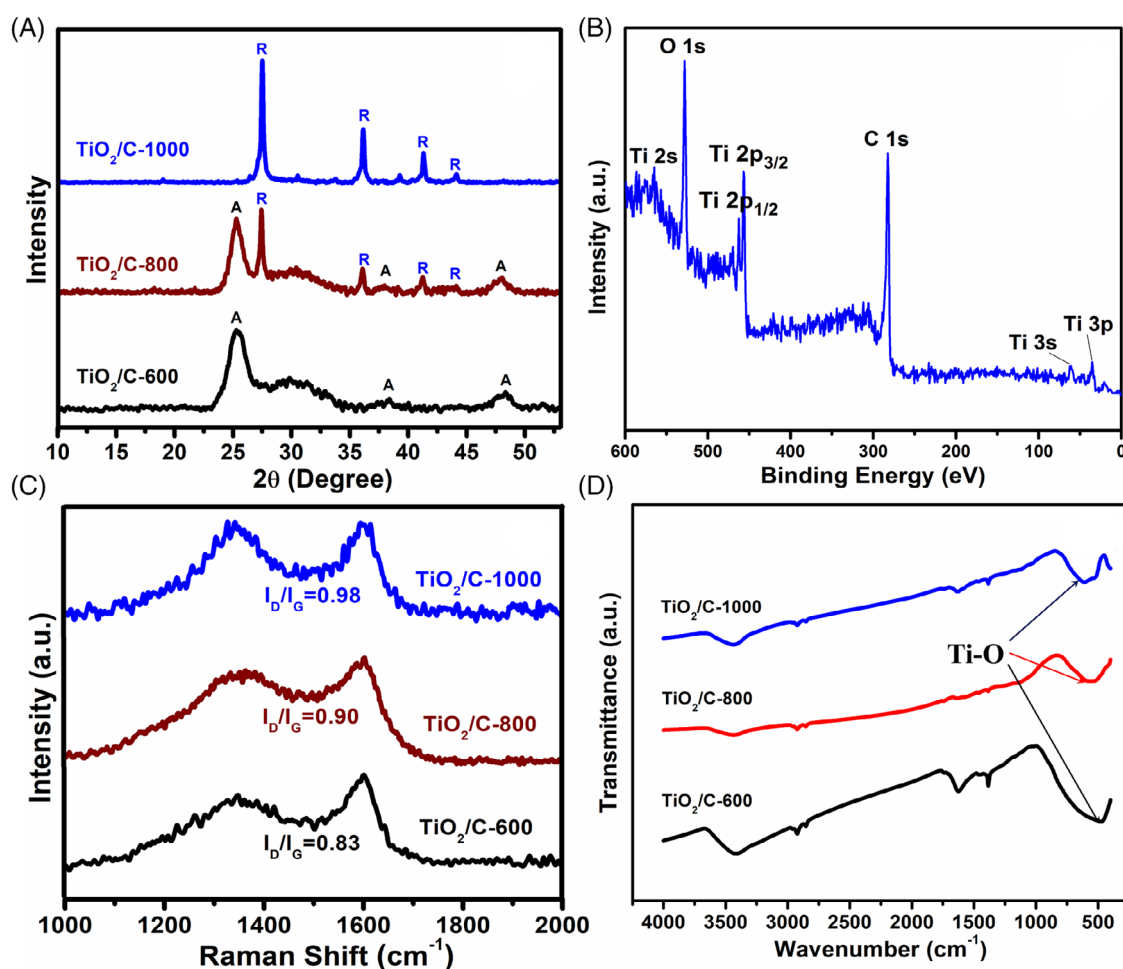


FIGURE 2 Spectral characterization of TiO₂/C composites: A, XRD spectra of the synthesized TiO₂/C composite at different pyrolysis temperatures. “A” and “R” indicate the anatase and rutile phases of TiO₂ respectively; B, XPS survey scan of TiO₂/C-1000; C, Raman spectra of the synthesized TiO₂/C composite at different pyrolysis temperatures; and D, FTIR spectra of TiO₂/C-1000, TiO₂/C-800 and TiO₂/C-600 [Colour figure can be viewed at wileyonlinelibrary.com]

increase in volume. Therefore, surface free energy plays crucial role during the crystallization of particular phase of the crystal. In particular, the change in surface free energy of the anatase phase is lower than that of the rutile phase. Alternatively, anatase phase needs less energy from the surrounding to form the stable nucleation surface than the rutile phase of TiO_2 .²⁸ Therefore, the anatase phase is more likely preferred to form at lower temperature than the rutile phase. Further, a progressive transition from anatase to rutile phase was evident at higher pyrolysis temperatures. TiO_2/C -800 contained a mixed-phase and partial emergence of the rutile phase was easily identified by the appearance of peaks at 27.3° , 36° , and 41.2° indexed to the (110), (101), and (111), respectively.²⁹ Although the transformation temperature for anatase to rutile is not unique, there are certain factors that affect (inhibit or promote) this transformation. Lattice rearrangements and transformations upon the removal of some atoms favor the kinetics of phase transition. The presence of carbon should greatly affect the phase transition temperature.³⁰ Ellingham diagram can be referred to here to correlate the temperature-dependent efficiency of carbon as a reducing agent.³¹ A decrease in Gibbs free energy of the system due to the copresence of carbon resulted in more oxygen vacancies even below the phase transition temperature of TiO_2 , which, in turn, brought down the structure rigidity to promote the phase transformation of TiO_2 .³⁰ The pyrolysis of MIL-125 (Ti) at 1000°C led to the formation of TiO_2/C composite wherein rutile phase was the predominant one. The fraction of two phases of TiO_2 (rutile and anatase) was evaluated using following equation

$$\frac{x_A}{x_R} = \frac{K_R}{K_A} \times \frac{I_A}{I_R} \quad (1)$$

Here, x_A and x_R are the mass fractions of anatase and rutile phase, respectively; likewise, I_A and I_R are the XRD peak intensities while K_A and K_R refer to the XRD peak intensity ratios.^{32,33} The effect of temperature on the fraction of anatase and rutile phases formed is given in Table 1. The rutile phase is known for its enhanced material stability compared to the anatase phase. Therefore, TiO_2/C -1000 material is expected to offer both desirable features of material stability (due to the Rutile phase) and electrical conductivity (due to conducting carbon content).

2.2 | Spectroscopic survey of materials

XPS survey was done to determine the chemistry of present species in TiO_2/C -1000 (Figure 2B). XPS analysis confirmed chemical bonding among oxygen (O) and titanium (Ti). The survey scan (Figure 2B) indicated the presence of O, Ti, and C atoms without any trace of impurities. Figure S3A represents the O 1s spectra, which is highlighted with three peaks at 527.2, 528.2, and 529.9 eV due to Ti—O—Ti, C—O—H, and Ti—O—H bonds, respectively.³⁴ On analyzing the carbon spectrum, the first two peaks demonstrate the presence of C—C (282 eV) and C=C (283 eV) bonds in the sample whereas the third peak at 283.7 eV reflects the presence of C—O bonds in the sample³⁵ (Figure S3B). Another visible peak at the bond dissociation energy of 285.3 eV is due to the Ti—O—C bond resulting from the pyrolysis of MIL-125 (Ti). Figure S3C represents the characteristics peaks of Ti 2p spectra with doublet splitting in Ti 2p_{3/2} (456.4 eV) and Ti 2p_{1/2} (462 eV).³⁶ A bond energy peak at 527.2 eV confirms the bonding between titanium and oxygen atoms.

Energy-dispersive X-ray spectroscopy (EDS) was further performed to investigate the percentage of carbon (given in Table 1) in the sample pyrolyzed at different temperatures (Figure S4). The percentage of the carbon atoms in comparison to titanium and oxygen is found increased. The presence of Ti peak at 4.5 keV and oxygen peak at 0.5 keV confirms their respective presence. Elemental atomic and weight % are given in Table S1. The weight percentage of the titanium decreases with the increase in temperature, which can also be evaluated from the TGA curve in which a slight decrease in weight can be observed even after the complete collapse of the MOF structure.

2.3 | Raman and FTIR spectroscopic investigations

Raman spectra of TiO_2/C composites are shown in Figure 2C. These spectra were recorded from 1000 to 2000 cm^{-1} to verify the presence of carbon content in the composite. Two broad Raman shifts at 1344 and 1594 cm^{-1} are referred to well-known D and G bands, respectively.^{37,38} Thus, Raman spectroscopic analyses

TABLE 1 Important material characteristics of different TiO_2/C samples derived from MIL-125 (Ti)

Samples	Rutile to Anatase phase ratio (%)	I_D/I_G	S_{BET} (m^2/g)	Pore Volume ($\text{cm}^3\text{ g}^{-1}$)	Carbon Percentage
TiO_2/C -600	0	0.83	48.16	0.0468	32
TiO_2/C -800	52.36	0.9	185.89	0.1956	36
TiO_2/C -1000	98.5	0.98	265.19	0.3586	46

were successful to verify the presence of carbon in the synthesized composites. Another analysis includes the increment of D and G band intensity ratio (0.83-0.9) with increases in pyrolyzing temperature (600°C-1000°C, respectively). This increase in intensity ratio suggests that the defects also increase in the carbon structure with temperature. It was also noted that the width of the D-band expands with the sample pyrolysis temperature (600°C-1000°C). The width of D peak is directly related to the distorted aromatic rings in graphitic layers while its broadening is related to the distortion of aromatic rings of the carbon. Hence, the sharpening of the D band at high pyrolysis temperatures (eg, TiO₂/C-1000) indicated the transition of high order aromatic carbon ring to six-membered aromatic carbon rings. Both the above observations on an increasing I_D/I_G ratio and a sharpened D band were comparable to the phase transformation of carbon from amorphous to nanocrystalline graphite with increasing defects.³⁸

FTIR spectra of different TiO₂/C composite samples are shown in Figure 2D. A common band around 3400 cm⁻¹ in all three samples is due to the O-H bond as different samples could adsorb water molecules from the environment when stored under ambient conditions after their synthesis. A band around 1629 cm⁻¹ is due to the combined effect of O-H bending vibration of chemically adsorbed water and C=C skeletal vibrations from graphitic domains. An absorbance band around 600 cm⁻¹ explains bond stretching harmonic motion in between

the Ti and O atoms of TiO₂³⁹ while sharpening of the said peak at a higher pyrolysis temperature (eg, at 1000°C) indicates the increasing relative purity of TiO₂ in the formed composite.

2.4 | Morphological analysis

The surface morphology is a crucial material parameter with regard to the application as an electrode for SCs.⁴⁰ Favorable surface morphology can facilitate electrode-electrolyte interactions.^{3,40,41} Figure 3 shows the FE-SEM analysis of the synthesized TiO₂/C-1000 composite sample. Carbon particles were spherical and almost homogeneous in their dimensions (submicron) with noticeable surface roughness. Their particle size ranged between 0.5 and 2 μm. TiO₂ nanoparticles were found to be distributed over and inside the carbon structure. Note that the titanium atoms form complex with the organic ligands and get uniformly distributed in MIL-125. During the pyrolysis of MIL-125 in Ar atmosphere, with the rise in temperature, the titanium bonds with organic linkers break down and react with oxygen atoms (provided by the BDC linker) to form TiO₂ nanoparticles. The advantage of this route of synthesis can be considered from the fact that the uniformly distributed titanium metal gets converted to TiO₂ nanoparticles which are still uniformly distributed inside the pores of the carbon structure. This explanation is further supported by the FESEM image of the

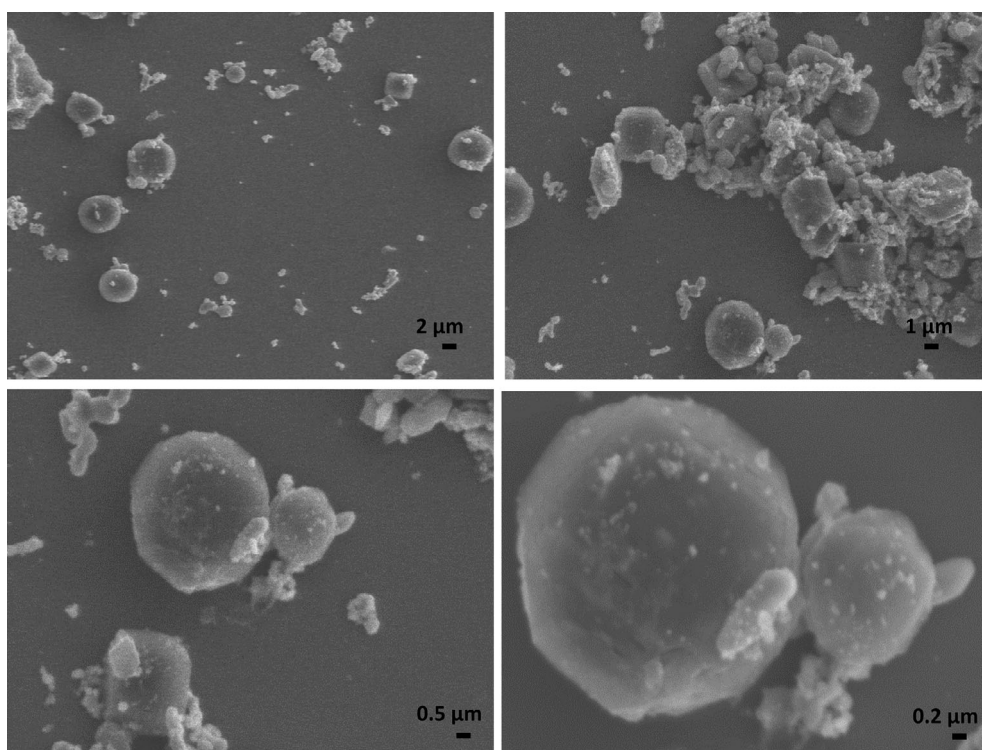


FIGURE 3 FE-SEM images of TiO₂/C-1000 at different magnifications

TiO₂/C-1000, in which TiO₂ nanoparticles found to come out from the spherical carbon. The spherical-shaped morphology of TiO₂/C-1000 composite should facilitate electrochemical performance due to the enhanced chances of efficient ion transport during the charging/discharging process.²⁵ For reference, a FESEM image of MIL-125(Ti) is provided in Figure S5. Similar to TiO₂/C-1000, the average size of the MIL-125(Ti) MOF found with a diameter range of 0.5 to 2 μm.

2.5 | BET surface area analysis

The surface area calculation and analysis are done using N₂ adsorption-desorption isotherms (Figure 4). The curve for the TiO₂/C-600 sample followed a typical type I sorption. This type I isotherm curve is governed by a steep increase at low pressure with no hysteresis loop during adsorption-desorption behavior. This behavior suggested that the material predominantly contained micropores (Figure 4A).⁴² The samples pyrolyzed at higher temperatures (TiO₂/C-800 and TiO₂/C-1000) were characterized by a Type IV isotherm indicating the presence of micro-mesopores.⁴³ In this context, the isotherm collected for the TiO₂/C-1000 sample exhibited more pronounced hysteresis when compared to other samples, that is, TiO₂/C-600 and TiO₂/C-800. A higher degree of hysteresis in the absorption/desorption isotherms in TiO₂/C-1000 is likely to reflect an enhanced meso-to-micropore ratio relative to other composite forms (ie, TiO₂/C-600 and TiO₂/C-800). The specific surface area of TiO₂/C-1000 was calculated to 265 m²/g, significantly higher than others (ie, 185 m²/g (TiO₂/C-800) and 48 m²/g (TiO₂/C-600)). Further to investigate the

fraction of meso-micro and macro pores in the sample, Barrett Joyner Halenda (BJH) plots have been analyzed (Figure 4B). The pores of the TiO₂/C-1000 sample mostly lie in the mesopores range (1-5 nm) centered at 2 nm. As seen from the above results, TiO₂/C-1000 was characterized by a better distribution of meso to micropores unlike the other two samples, that is, TiO₂/C-600 and TiO₂/C-800. Therefore, the application of TiO₂/C-1000 should be advantageous as it would likely support better transport of electrolytic ions via shorter diffusion paths.

2.6 | Electrochemical performance of TiO₂/C composite

Based on the material characterization results (as discussed in the preceding sections), TiO₂/C-1000 was finally selected as a SC electrode material for detailed analysis in this research. Comparative cyclic voltammetry (CV) characteristics of different samples (TiO₂/C-1000, TiO₂/C-800, TiO₂/C-600) are presented in Figure S6A. Here also, based on these preliminary studies, it can be inferred that the TiO₂/C-1000 sample would provide the best values of capacitance.

Figure 5A represents the CV curves of the TiO₂/C-1000 sample which are found to be of rectangular shape without obvious redox peaks. This typical EDLC behavior, supporting the well-known relation of $I(t) = C(dV/dt)$, could be attributed to the presence of carbon in the composite.⁴⁴ Nonetheless, a small redox peak also appeared at slow scan rates (1-5 mV/s) attributed to the copresence of TiO₂ particles as redox-active species in the electrode material. The appearance of this redox peak

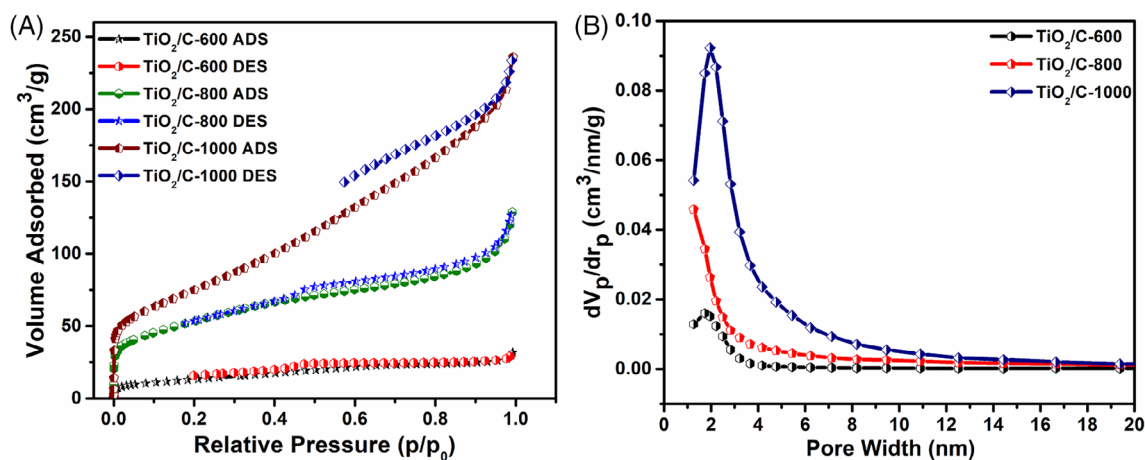


FIGURE 4 Surface area and pore size distribution analysis of TiO₂/C-1000, TiO₂/C-800, and TiO₂/C-600. A, N₂ adsorption-desorption isotherms; B, BJH pore size distribution plots for TiO₂/C-600, TiO₂/C-800, and TiO₂/C-1000 samples [Colour figure can be viewed at wileyonlinelibrary.com]

also suggested that the selected system should have a high energy density.^{33,45} As such, the present TiO₂/C-1000 composite electrode-based SC has combined EDLC and Faradaic types of charge storage mechanisms to result in a system with features of both high charge storage capacity and their fast deliveries when needed.

Further, the C_s of the electrode material was calculated using derived calculations provided in Supporting information (Equation S1). From CV curves, the sample @1000°C delivers the C_s value of 314 F/g @ 1 mV/s. A decline in the C_s value of the system was observed with increases in the scan rate (Figure S7A). This effect became more apparent when the system ran at fast scan rates. It is because of the fact that at fast scan rates the electrolyte ions are able to partially only access the reaction sites on the surface of the electrode material. Therefore, the inability of electrolyte ions to

access reaction sites under fast voltage scans leads to a decrease in C_s value.

Further, CV data have been used to determine the mechanism of charge storage by the TiO₂/C-1000 electrode. For this, a logarithmic plot of peak current vs scan rate was prepared (Figure 5B). The linearity relationship of the data plotted in Figure 5B satisfied the following power-law equations.^{46,47}

$$i_p = av^b \quad (2)$$

$$\log(i_p) = b \log(v) + \log a \quad (3)$$

The plots in Figure 5B have been used to compute the values of variables “a” and “b.” It may be highlighted here that the value “b” is taken as an indicator to

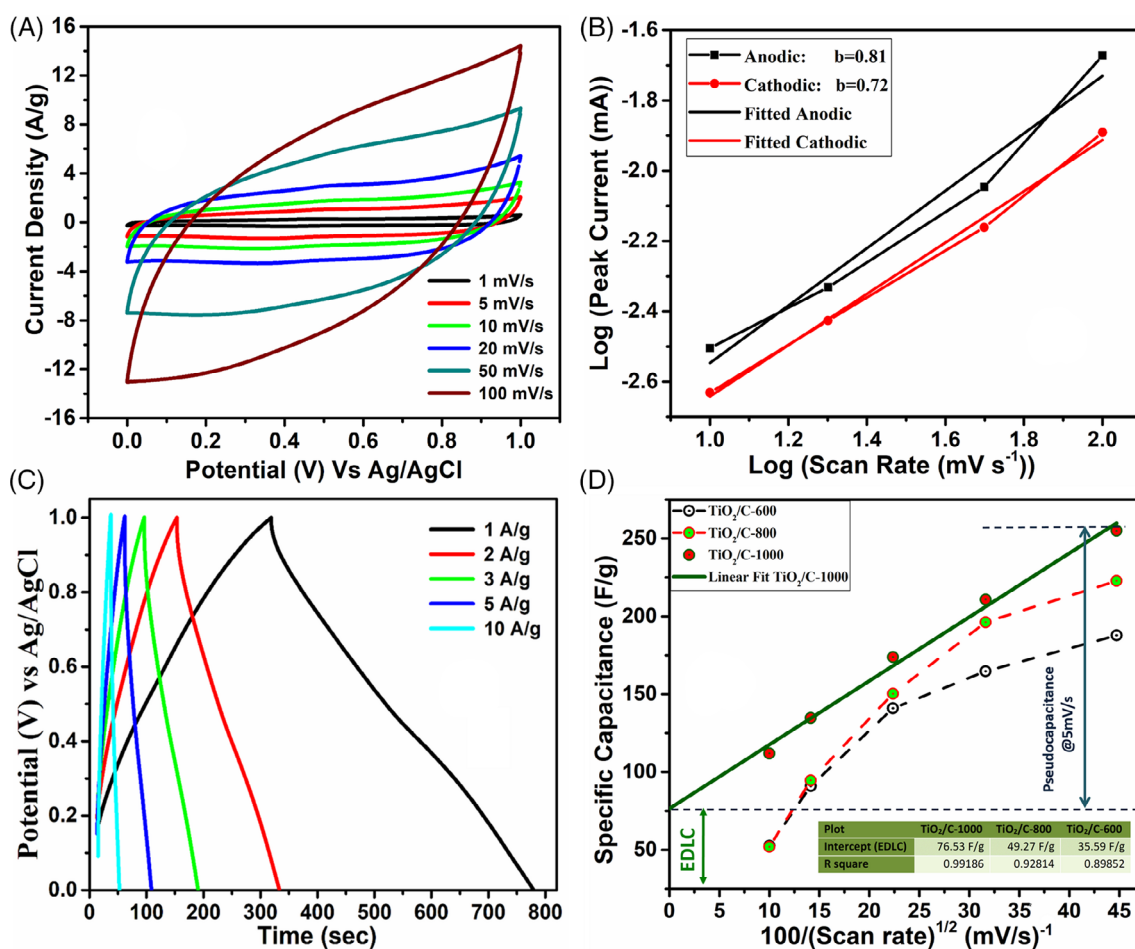


FIGURE 5 Electrochemical analysis for the evaluation of capacitive behavior of TiO₂/C-1000 electrode in three-electrode setup: A, CV curves for TiO₂/C-1000 electrodes using 1 M H₂SO₄ electrolytes at a scan rate of 1–100 mV/s; B, Logarithmic relation between peak current vs scan rate and determination of “b” value; C, GCD plots for TiO₂/C-1000 composite electrode at different current densities D, quantitative analysis of EDLC and pseudocapacitive behavior of TiO₂/C-1000, TiO₂/C-800, and TiO₂/C-600 [Colour figure can be viewed at wileyonlinelibrary.com]

determine the nature of processes involved in the charge storage mechanism. The “*b*” value of 0.5 indicates the involvement of a diffusion-controlled process. In contrast, $b = 1$ would point toward capacitive reactions over the electrode–electrolyte interface as the capacitive current shows a directly proportional relationship with respect to the sweep rate.⁴⁶ The “*b*” values for the cathodic and anodic peak current presented in Figure 5B have been estimated as 0.72 and 0.81, respectively, which are close to 1. Hence, these values confirm the predominance of a capacitive type of charge storage process, which also contributes to the fast charge transfer.⁴⁸

Figure 5C shows the effect of increasing current density over the charging/discharging time. These patterns with typical linearity and a very small voltage drop are clearly indicative of the system possessing a low internal resistance.⁴⁹ Furthermore, a linear discharge curve suggested the predominant EDLC characteristic of the electrode. Additionally, a small bend in the discharging curve also signified the involvement of Faradaic reactions in the system owing to the copresence of TiO₂. This behavior can be related to the same activities happening at fast scan rates (described in CV analysis). At such high current density, the electrolyte ions did not get enough time to access all the inner part of the electrode material.⁵⁰ This excellent electrochemical performance can be attributed to the presence of redox-active species and well-distributed carbon pores. For comparison purposes, the galvanostatic charge-discharge (GCD) plots for the three different synthesized electrode materials are given in Figure S6B. Among them TiO₂/C-1000 demonstrate the maximum discharge time demonstrate the higher specific capacitance than the other two samples. Apart from this, the open circuit potential (OCP) for sample TiO₂/C-1000 is 0.42 V (vs Ag/AgCl). Therefore, above 0.42 V the sample will show charging/discharging curve in the positive potential window and below 0.42, the sample will show charging/discharging curve in the negative potential window. The 100% coulombic efficiency (CE) was calculated for the sample in positive potential window however this CE decreases below 100% when the sample enters in negative potential window (shown in Figure S8). Thus, the sample takes higher time when the potential of the sample changes from 1 to 0 V (vs Ag/AgCl) as compared to potential changes from 0 to 1 V. For simplicity, Figure S8 demonstrates the different charging and discharging time in the positive and negative potential window.

For further quantitative analysis of the EDLC (absorption of ions) and pseudocapacitive behavior (redox reactions and diffusion of electrolyte in the pores of active material), the variation of the total capacitance per electrode (C_T) with respect to $s^{-1/2}$

(s = scan rate) has been accounted (Figure 5D). It can be clearly seen that the proportion of pseudocapacitive contribution in total capacitance decreases as the scan rate is increased. It may be noted that pseudocapacitive processes take place as a result of Faradaic reactions at the surface of active material (ie, electrode material). Pseudocapacitance is a relatively slow process compared to EDLC. Therefore, higher scan rates, as well as fast discharge conditions, may lead to weakened pseudocapacitive properties, which, in turn, are also reflected in an attenuated value of total capacitance per electrode (C_T).⁵¹ In other words, high scan rates would not allow maximum output from the electrode due to hindrance in its pseudocapacitive property. Such a situation is characterized by a nonlinear relationship between C_T and $s^{-1/2}$.⁵² However, the present TiO₂/C-1000 electrode has delivered an almost linear behavior for C_T vs $s^{-1/2}$ (Figure 5D). Therefore, the TiO₂/C-1000 electrode can deliver unabridged SC performance even at high scan rates. As the linear fit model in (Figure 5D) has revealed, the EDLC mechanism contributed 76 F/g out of the total 258 F/g (5 mV/s). The rest of the capacitance (ie, 182 F/g, around 70% of the total capacitance) is driven by the pseudocapacitive mechanism. In contrast, the TiO₂/C-600 and TiO₂/C-800 electrode-based devices yielded non-linear behaviors under high scan rate conditions (Figure 5D). An estimation of pseudocapacitive and EDLC contributions with the use of TiO₂/C-600 and TiO₂/C-800 is also provided in Figure 5D. The linear fit curves for TiO₂/C-600 and TiO₂/C-800 (Figure S9A,B). Compared to TiO₂/C-1000 electrode (182 F/g), TiO₂/C-800 and TiO₂/C-600 yielded lesser values of pseudocapacitance, that is, 164 and 152 F/g, respectively. The superior pseudocapacitive nature of TiO₂/C-1000 can be associated with it bearing an improved distribution of meso and micropores as compared with the other two processed materials.

Apart from the better pseudocapacitance, TiO₂/C-1000 is also characterized by a better EDLC characteristic (76 F/g) than TiO₂/C-800 (49 F/g) and TiO₂/C-600 (35 F/g). This factor is explained by the relatively higher surface area of TiO₂/C-1000 compared to the other two materials. An enhanced electrode/electrolyte interfacial contact region allowed the TiO₂/C-1000 electrode to deliver better EDLC nature as well.

As both CV and GCD investigations have revealed, the TiO₂/C-1000 electrode delivered remarkably enhanced specific capacitance, attributable to considerable ionic conductance through the presence of active sites in the carbon structure.⁵⁰ The cyclic stability of the TiO₂/C-1000 electrode has also been investigated (Figure S10). After 2000 charging discharge cycles, the present system retained excellent capacitance retention of 95%, clearly indicating the potential practical usability of our SC design. Further, the EIS characterization has been carried out to investigate

the resistance generated during charge transfer at the interface of electrode/electrolyte of the TiO₂/C-1000. The recorded EIS curves (Nyquist plots) displayed an almost linear pattern with a negligible semicircle shape (Figure S11). Accordingly, the TiO₂/C-1000 electrode should have operated with little charge transfer resistance (ESR = 7 Ω). Such a significant conductive nature of the electrode material can be attributed to the presence of carbon in the composite material, which helps to minimize the electrode/electrolyte interfacial resistance consequently leading to fast charge transfer.⁵³ Further, the effect on C_s value of the electrode material with different mass loading has been studied. Four different electrodes have been prepared with a mass loading of 1, 2, 3 and 4 mg/cm². The GCD curves of all the four electrodes at 3 A/g are shown in Figure S12A. The discharging time, measured at a constant areal current density of 3 mA/cm², shows an increase with the increasing mass loading. Accordingly, the specific gravimetric capacitance shows a decrease. This behavior is caused by the inability of the electrolyte ions to access the inner part (called dead area) of the electrode material.¹⁷ An increased mass loading also caused more thick material layering over the electrode surface. Under such conditions, the whole TiO₂/C material (particularly inner part) would not be efficiently usable during fast charging–discharging processes. The gravimetric and areal capacitance at different mass loadings have been calculated and given in Figure S12B and S12C. The detailed discussion of mass loading effect over

areal and gravimetric capacitance is also mentioned in Supporting information.

A comparison of the present system with similar SC designs reported previously has been summarized in Table 2. Based on the available data, the TiO₂/C-1000 electrode system can be projected to possess the excellent potential to develop highly efficient SCs. This impregnation of TiO₂ nanoparticle provides extra stability towards its dissolution in the electrolyte. Moreover, the volume change of the TiO₂ nanoparticles due to their redox activity can be overcome with a flexible carbon matrix. Thus, the outstanding electrochemical performance of the TiO₂/C-1000, when compared to the composites used in the literature, is attributed to the novel synthesis route which provides the effective infused TiO₂ nanoparticles in the pores of carbon network.

2.7 | Performance analysis of TiO₂/C-1000//TiO₂/C-1000 symmetrical SC

The aforementioned results derived with a three-electrode SC system highlight the practical applicability of the hybrid TiO₂/C-1000 composite electrode. The investigations were further extended to evaluate the performance of symmetrical SC, fabricated using two equally weighted TiO₂/C-1000 electrodes (two-electrode cell configuration, 0.95 mg material over each electrode). For this

TABLE 2 A comparison of supercapacitor performance parameters of the MIL-125 (Ti)-derived TiO₂/C electrode with previously reported metal-organic framework (MOF)-derived NPC composites and TiO₂ composites electrodes

S. No.	Electrode Material	Electrolyte	Scan rate/Current Density	Specific Capacitance (F/g)	Ref.
1	MOF-5-derived NPC	1 M H ₂ SO ₄	5 mV/s	167	49
2	MOF-5-derived NPC	1 M H ₂ SO ₄	1 mV/s	236	50
3	TE-MOF-5-derived NPC	6 M KOH	0.25 A/g	271	54
4	MOF-2-derived NPC	1 M H ₂ SO ₄	1 A/g	170	51
5	HKUST-1-derived NPC	3 M KOH	0.1 A/g	143.3	52
6	ZIF-8-derived NPC	0.5 M H ₂ SO ₄	5 mV/s	214	53
7	ZIF-8-derived NPC	1 M H ₂ SO ₄	5 mV/s	251	13
8	ZIF-69-derived NPC	0.5 M H ₂ SO ₄	5 mV/s	168	55
9	Zn-BTC-derived NPC	1 M H ₂ SO ₄	1 A/g	134	51
10	MOF-5-derived NPC	6 M KOH	0.1 A/g	121.3	52
11	N-doped ZIF-8-derived NPC	6 M KOH	0.1 A/g	258.5	56
12	N-doped ZIF-11-derived NPC	1 M H ₂ SO ₄	1 A/g	307	57
13	rGO/TiO ₂ nanofibers aerogels	1 M Na ₂ SO ₄	1 A/g	178	58
14	TiO ₂ /Graphene hydrogel	1 M Na ₂ SO ₄	0.5 A/g	206	59
15	rGO/TiO ₂ nanobelts	1 M Na ₂ SO ₄	0.125 A/g	225	60
	rGO/TiO ₂ NPs			62.8	
16	MIL-125 (Ti)-derived TiO ₂ /C	1 M H ₂ SO ₄	5 mV/s	258	This work

device, we preferred an electrolyte prepared by infiltrating a polymer gel with 1 M H₂SO₄. The resulting polymer gel electrolyte is likely to offer certain important device advantages such as flexibility, leakage-free operation, and a wide potential window.⁵⁵ The polymer gel electrolyte has been deployed as a separator and electrolyte between the two identical electrodes to assemble a solid-state symmetrical SC.

The first thing to do with the fresh assembled symmetrical SC is to determine its operating voltage window.^{40,61} This is because the voltage window of the device can affect various parameters (eg, C_s, energy density, and cycle life). For example, the energy density of the device is directly related to the square of the operating voltage of the device.⁴⁶ So, the higher the voltage window, the higher will be the energy density of the device. However, in this scenario, one should have kept the running device under the safe voltage window. If the device is working in a safe operating voltage window, it will have high energy density for a large number of

charging–discharging cycles. Keeping this in mind, the assembled device was scanned across different voltage windows to determine the decomposition point of electrolytes through CV curves collected from 0 to 1.8 V (Figure 6A). The obtained CV curves in this study suggest that the safe operating voltage of the assembled device is limited to 1.8 V. At such extreme voltage, the evolution of hydrogen and oxygen gas started due to the decomposition of electrolyte (electrolysis of water present in the electrolyte) at the electrode surface. This effect can be observed from the steep increase in CV current (Figure 6A). The operation of the device beyond this voltage window can nonetheless lead to device failure mainly due to the loss of ions during the evolution of hydrogen and oxygen gas at the surface of the electrode material. Also, the evolution of gas changes the molarity of the electrolyte, which can subsequently affect the operating voltage window of the device. Other snags of operating the device above its working voltage window include the irreversible redox reactions in the electrode material (at a higher voltage).

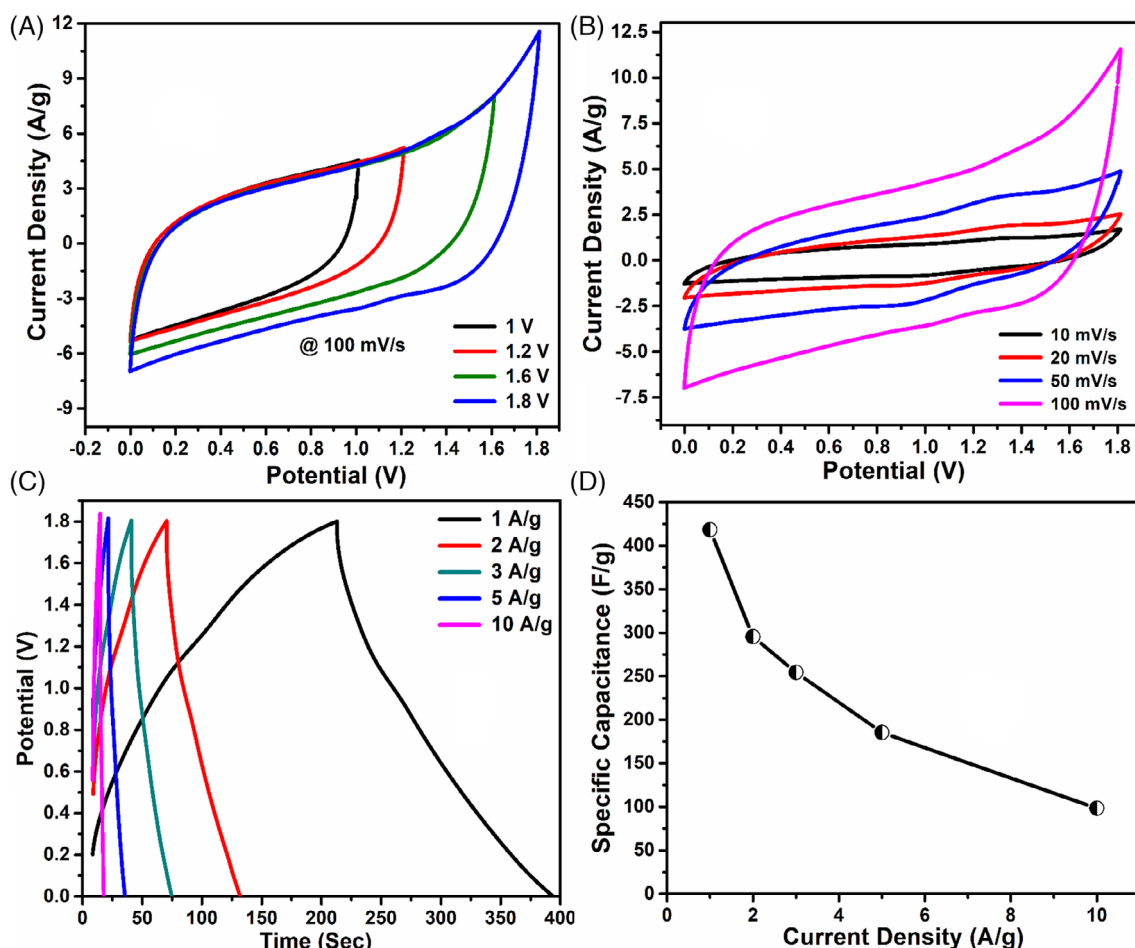


FIGURE 6 Electrochemical performance of TiO₂/C-1000//TiO₂/C-1000 symmetric supercapacitor in the presence of PVA-1 M H₂SO₄ polymer gel electrolyte: A, CV curves for various operating potential windows; B, CV curves at different scan rates from 10 to 100 mV/s; C, GCD plots at different current densities from 1.5 to 5 A/g; and D, Variation of specific capacitance as a function of current density [Colour figure can be viewed at wileyonlinelibrary.com]

This effect may not be prominent in the single course of charging–discharging cycles. However, with every subsequent cycle, the device started to lose the C_s value with a reduction in the energy density of the device. Therefore, the operation of the device above its safe voltage window to achieve high energy density may lead to the loss of charge storage capability after a few cycles of charging–discharging. Apart from this, while determining the true operating voltage window, one should also consider the voltage ranges for the maximum CV area which directly resembles the C_s of the device.⁵⁶ Therefore, the selection of voltage range with a maximum CV area (maximum I-V area coverage) is a crucial parameter to achieve the high electrochemical performance of the device (eg, high energy density). In our case, the curve with a 1.8 V window was found to attain the maximum IV area among other lower voltage windows. Also, the operation of the device above this voltage window range will be unsafe due to the steep increase in CV current at 1.8 V, which resembles the

starting of electrolyte decomposition. Further, the CV patterns at different scan rates for a device were typical, possessing an almost perfect rectangular behavior (Figure 6B). Here again, the appearance of a small redox peak (particularly at slow scan rates) could be ascribed to the contribution from TiO_2 -related Faradaic processes.

Figure 6C represents the charging–discharging curves at various current densities. The device exhibits the excellent electrochemical performance as expected from the three-electrode system analysis. The coulombic efficiency of the device was almost 100% as there was no significant difference between the charging and discharging times (Figure 6C). The C_s decreases with a decrease in current density as presented in Figure 6D. The same was also observed during the three electrode-based studies; the better C_s value was achievable for lower current densities.

An estimation of the quantitative contribution from among EDLC and pseudocapacitive behaviors for a single electrode of the device is made by plotting the capacitance values

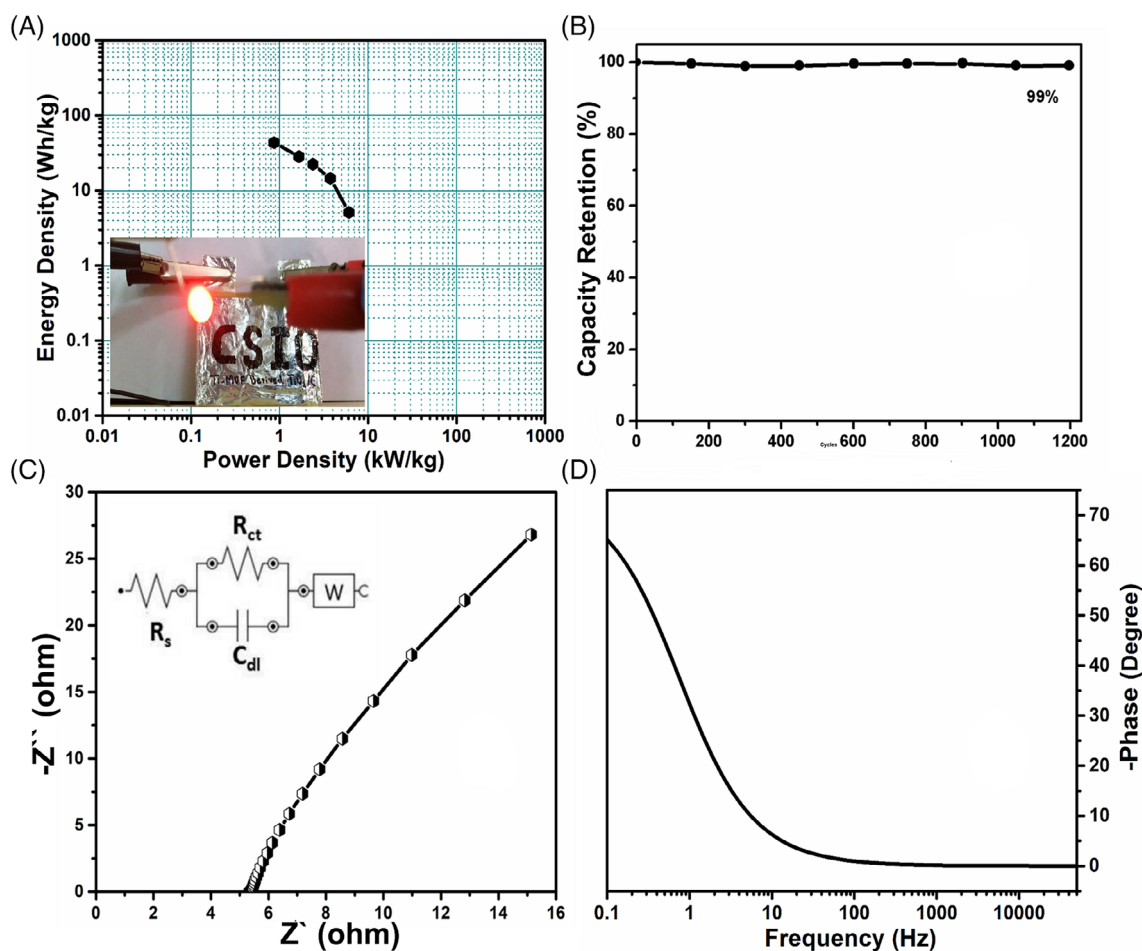


FIGURE 7 Investigations on energy density, cycle stability, and independence characteristics of the fabricated supercapacitor: A, Ragone plot (Inset showing two symmetrical supercapacitors combined in series to energize a white LED); B, Cyclic stability of $TiO_2/C-1000//TiO_2/C-1000$ device for 1200 cycles evaluated at a current density of 10 A/g; C, Nyquist plot (Inset showing equivalent circuit); D, Phase frequency curve for $TiO_2/C-1000$ based 1.8 V symmetric supercapacitor in the presence of PVA-1 M H_2SO_4 gel electrolyte [Colour figure can be viewed at wileyonlinelibrary.com]

with respect to the reciprocal of scan rates (Figure S13A). Based on the mathematical calculations, an EDLC value of 70 F/g per electrode is estimated for the symmetrical device. The above-calculated value is very close to the value (76 F/g) obtained from the three-electrode systems investigated in this work. In an ideal situation, both CV and GCD should yield comparable values of capacitance for the symmetrical device. This information has been deduced by plotting curves between values of capacitance and dV/dt collected at different current densities based on both CV and GCD methods (Figure S13B). It can be concluded from this analysis that the electrochemical behavior of the proposed symmetrical capacitor is fairly stable and reproducible as it is characterized by similar curve trends for both CV and GCD operations.

The two crucial parameters of energy storage devices are the energy density (E_s) and power density (P_s), which ultimately expose the real potential of a device. The two parameters of the assembled device were calculated using Equations S4 and S5. The deliverable energy density at different power rates is shown in the Ragone plot Figure 7A. The device attained the maximum E_s of 43.5 Wh/kg. This high E_s value was obtained when the device ran at the power output (P_s) of 0.865 kW/kg. However, with the increase in the rate of energy deliveries (P_s), the E_s decreased. The same trend is plotted in Ragone plot, that is, with increases in the power output values (P_s), the E_s value decreases. The acquisition of these excellent device parameters suggests the potential practical applications of the herein proposed SC design (TiO₂/C-1000//TiO₂/C-1000). Furthermore, the device was capable of retaining almost 99% of its C_s even after 1200 charge-discharge cycles (Figure 7B).

EIS characteristics of the TiO₂/C-1000//TiO₂/C-1000 device is presented in Figure 7C (Nyquist plot) and Figure 7D (phase relationship). The ESR (effective series resistance) and R_{ct} (charge transfer resistance) values were calculated as 5.33 and 0.179 Ω , respectively, from Nyquist plot. The equivalent circuit is given in the inset of Figure 7C. These parameters reveal the excellent conductivity of the device. An almost ideal SC behavior was evident from the maximum phase observed at 70°. Nonetheless, a little deviation from the ideal SC behavior was probably due to the presence of TiO₂, which caused partial pseudocapacitance.

As such, the excellent capacitive performance, cyclic stability, and energy storage capability of the herein proposed TiO₂/C composites assembled device can be ascribed to two main synergistic factors, for example, (a) coinvolvement of two types of charge-storage mechanisms, that is, predominant EDLC (carbon nature) and redox activity of TiO₂ nanoparticles and (b) conducting and porous nature of TiO₂/C network, which allowed the device to perform with little R_{ct} values and efficient diffusion of electrolyte ions at the electrode-electrolyte interface.

3 | CONCLUSIONS

This work was carried out to demonstrate the potential utility of hybrid TiO₂ nanoparticles infused in carbon pores for the application in supercapacitor. The controlled pyrolysis of Ti-MOF (MIL-125) at 1000°C has guaranteed a porous structure containing both meso and micropores apart from also being highly electrically conducting. The sample TiO₂/C@1000°C with rutile phase was found to exhibit higher electrochemical performance than the other two samples pyrolyzed at 800°C and 600°C with mixed and anatase phases, respectively. TiO₂/C@1000°C sample attained the highest specific surface area of 265 m²/g. TiO₂/C@1000°C electrode has yielded a C_s value of 258 F/g at 5 mV/s of scan rate. On the same line, the assembled device exhibited a high energy density of 43.5 Wh/kg at a power density of 865 W/kg. Apart from this, the reversible redox reactions over the surface of the TiO₂ fraction resulted in an additional advantage of pseudocapacitance, which yielded high energy density from the device. The TiO₂/C-1000 electrode can be developed as a single symmetrical device or can be combined in series for high voltage applications. This idea of using uniformly infused metal oxide in the carbon matrix can further be elaborated to control the fraction of the rutile phase in the carbon matrix. The effect of varying fraction of the rutile phase in the carbon matrix deserves to be explored in more details. Acknowledging this approach as an effective route to obtain well-dispersed nanoparticles in a carbon matrix, different types of other pseudocapacitive hybrid material can be realized and investigated for energy storage application.

ACKNOWLEDGMENTS

The authors (Vishal Shrivastav and Shashank Sundriyal) acknowledge the UGC (university grant commission) for their fellowship and Director, CSIR-CSIO to provide facilities. This research also acknowledges research and development Centre for Global Top Environmental Technologies and Green Patrol Technologies funded by the Ministry of Environment (Grant No. 2018001850001) as well the funding bodies Ministry of science to provide funds for National Research Foundation of Korea (NRF) (Grant No: 2016R1E1A1A01940995). This research also acknowledges Cooperative Research Program for Agriculture Science & Technology Development (Project No. PJ014297) funded by Rural Development Administration, Republic of Korea. This work also acknowledges CSIR, India projects MLP-023 and MLP-0029.

ORCID

Umesh K. Tiwari  <https://orcid.org/0000-0002-4641-3391>

REFERENCES

- Karami N, Moubayed N, Outbib R. Analysis and implementation of an adaptative PV based battery floating charger. *Sol Energy*. 2012;86:2383-2396.
- Yang K, Cho K, Kim S. Effect of carbon black addition on thermal stability and capacitive performances of supercapacitors. *Sci Rep*. 2018;8:11989.
- Sundriyal S, Kaur H, Bhardwaj SK, Mishra S, Kim K-H, Deep A. Metal-organic frameworks and their composites as efficient electrodes for supercapacitor applications. *Coord Chem Rev*. 2018;369:15-38.
- Tamme R, Bauer T, Buschle J, Laing D, Müller-Steinhagen H, Steinmann WD. Latent heat storage above 120°C for applications in the industrial process heat sector and solar power generation. *Int J Energy Res*. 2008;32:264.
- Hiesgen R, Wehl I, Aleksandrova E, Roduner E, Bauder A, Friedrich KA. Nanoscale properties of polymer fuel cell materials—a selected review. *Int J Energy Res*. 2010;34:1223.
- Mainar AR, Leonet O, Bengoechea M, et al. Alkaline aqueous electrolytes for secondary zinc-air batteries: an overview. *Int J Energy Res*. 2016;40:1032-1049.
- Azman NHN, Mamat MS, Nazir M, Ngee LH, Sulaiman Y. Graphene-based ternary composites for supercapacitors. *Int J Energy Res*. 2018;42:2104.
- Sundriyal S, Sharma M, Kaur A, Mishra S, Deep A. Improved electrochemical performance of rGO/TiO₂ nanosheet composite based electrode for supercapacitor applications. *J Mater Sci Mater Electron*. 2018;29:12754.
- Xiong H, Slater MD, Balasubramanian M, Johnson CS, Rajh T. Amorphous TiO₂ nanotube anode for rechargeable sodium ion batteries. *J Phys Chem Lett*. 2011;2:2560. Su D, Dou S, Wang G. Anatase TiO₂: better anode material than amorphous and rutile phases of TiO₂ for Na-ion batteries. *Chem Mater*. 2015;27:6022.
- Yang X, Wang C, Yang Y, et al. Anatase TiO₂ nanocubes for fast and durable sodium ion battery anodes. *J Mater Chem A*. 2015;3:8800. Chen C, Wen Y, Hu X, et al. Na⁺ intercalation pseudocapacitance in graphene-coupled titanium oxide enabling ultra-fast sodium storage and long-term cycling. *Nat Commun*. 2015;6:6929. Zhang Y, Foster CW, Banks CE, et al. Graphene-rich wrapped petal-like rutile TiO₂ tuned by carbon dots for high-performance sodium storage. *Adv Mater*. 2016;28:9391. Zhang Y, Yang Y, Hou H, et al. Enhanced sodium storage behavior of carbon coated anatase TiO₂ hollow spheres. *J Mater Chem A*. 2015;3:18944.
- Lazarte JPL, Dipasupil RC, Pasco GYS, et al. Synthesis of reduced graphene oxide/titanium dioxide nanotubes (rGO/TNT) composites as an electrical double layer capacitor. *Nanomaterials*. 2018;8:934.
- Pant B, Park M, Park S-J. TiO₂ NPs assembled into a carbon nanofiber composite electrode by a one-step electrospinning process for supercapacitor applications. *Polymers*. 2019;11:899.
- Eltom A, Zhong G, Muhammad A. Scaffold techniques and designs in tissue engineering functions and purposes: a review. *Adv Mater Sci Eng*. 2019;2019:1-13.
- Elmouwahidi A, Bailón-García E, Castelo-Quibén J, Pérez-Cadenas A, Maldonado-Hódar F, Carrasco-Marín F. Carbon-TiO₂ composites as high-performance supercapacitor electrodes: synergistic effect between carbon and metal oxide phases. *J Mater Chem A*. 2018;6:633-644.
- Tang K, Li Y, Cao H, Su C, Zhang Z, Zhang Y. Amorphous-crystalline TiO₂/carbon nanofibers composite electrode by one-step electrospinning for symmetric supercapacitor. *Electrochim Acta*. 2016;190:678. Jo H, Jung M-J, Kim KH, Lee Y-S. *Carbon Lett*. 2018;27:64. Yue HY, Guan EH, Gao X, et al. Hydrothermal synthesis of TiO₂ nanowires-reduced graphene oxide nanocomposite to enhance electrochemical performance in supercapacitor. *ChemistrySelect*. 2018;3:12455.
- Lu Y, Yan H, Zhang D, et al. Hybrid nanonet/nanoflake NiCo₂O₄ electrodes with an ultrahigh surface area for supercapacitors. *J Solid State Electrochem*. 2014;18:3143. Sun T, Hu J, Ren X, Wang S. Experimental evaluation of the adsorption, diffusion, and separation of CH₄/N₂ and CH₄/CO₂ mixtures on Al-BDC MOF. *Sep Sci Technol*. 2015;50:874. Bloch ED, Queen WL, Krishna R, Zdrozny JM, Brown CM, Long JR. Hydrocarbon separations in a metal-organic framework with open iron(II) coordination sites. *Science*. 2012;335:1606. Shrivastav V, Sundriyal S, Goel P, et al. Metal-organic frameworks (MOFs) and their composites as electrodes for lithium battery applications: Novel means for alternative energy storage. *Coord Chem Rev*. 2019;393:48.
- Salunkhe RR, Kamachi Y, Torad NL, et al. Fabrication of symmetric supercapacitors based on MOF-derived nanoporous carbons. *J Mater Chem A*. 2014;2:19848-19854.
- Liao Y-T, Matsagar BM, Wu KC-W. Metal-organic framework (MOF)-derived effective solid catalysts for valorization of lignocellulosic biomass. *ACS Sustainable Chem Eng*. 2018;6:13628. Wu K, Yang M, Pu W, Wu Y, Shi Y, Hu H-s. Carbon promoted ZrO₂ catalysts for aqueous-phase ketonization of acetic acid. *ACS Sustainable Chem Eng*. 2017;5:3509. Kamyar N, Rezaee S, Shahrokhian S, Amini MM. Direct conversion of inorganic complexes to platinum/thin oxide nanoparticles decorated on MOF-derived chromium oxide/nanoporous carbon composite as an efficient electrocatalyst for ethanol oxidation reaction. *J Colloid Interface Sci*. 2019;555:655.
- Bhadra BN, Song JY, Khan NA, Jhung SH. TiO₂-containing carbon derived from a metal-organic framework composite: a highly active catalyst for oxidative desulfurization. *ACS Appl Mater Interfaces*. 2017;9:31192.
- Wang P, Lang J, Liu D, Yan X. TiO₂ embedded in carbon submicron-tablets: synthesis from a metal-organic framework precursor and application as a superior anode in lithium-ion batteries. *Chem Commun*. 2015;51:11370-11373.
- Shi X, Zhang Z, Du K, Lai Y, Fang J, Li J. Anatase TiO₂@C composites with porous structure as an advanced anode material for Na ion batteries. *J Power Sources*. 2016;330:1-6.
- Vilela S, Salcedo-Abraira P, Colinet I, et al. Nanometric MIL-125-NH₂ metal-organic framework as a potential nerve agent antidote carrier. *Nanomaterials*. 2017;7:321.
- Dan-Hardi M, Serre C, Frot T, et al. A new photoactive crystalline highly porous titanium(IV) Dicarboxylate. *J Am Chem Soc*. 2009;131:10857-10859.
- Li X, Pi Y, Hou Q, et al. Amorphous TiO₂@NH₂-MIL-125 (Ti) homologous MOF-encapsulated heterostructures with enhanced photocatalytic activity. *Chem Commun*. 2018;54:1917-1920.

25. Wang W, Wang Z, Liu J, et al. Single-step one-pot synthesis of TiO₂ Nanosheets doped with Sulfur on reduced graphene oxide with enhanced photocatalytic activity. *Sci Rep.* 2017;7: 46610.
26. Matthews A. *Am Mineral.* Effect of grain size on structural transitions in anatase TiO₂: A Raman spectroscopy study at high pressure. 1976;61:419.
27. Çelikkilek M, Ersundu AE, Aydın S. The crystallization of anatase and rutile from amorphous titanium dioxide under hydrothermal conditions. *Adv Cryst Processes.* 2012;127:419-424.
28. Ghosh T, Dhabal S, Datta A. On crystallite size dependence of phase stability of nanocrystalline TiO₂. *J Appl Phys.* 2003;94:4577.
29. Gu Y, Cheng K, Wu Y-n, Wang Y, Morlay C, Li F. Metal-organic framework-templated synthesis of bifunctional N-doped TiO₂-carbon nanotables via solid-state thermolysis. *ACS Sustainable Chem Eng.* 2016;4:6744. Guo Z, Cheng JK, Hu Z, et al. Metal-organic frameworks (MOFs) as precursors towards TiOx/C composites for photodegradation of organic dye. *RSC Adv.* 2014;4:34221.
30. Hanaor DA, Sorrell CC. Review of the anatase to rutile phase transformation. *J Mater Sci.* 2011;46:855.
31. Hasegawa M. *Treatise on Process Metallurgy.* Oxford, UK: Elsevier; 2014:1:507.
32. Johnson Q, Zhou R. Phase identification using whole-pattern matching. *Adv X-Ray Anal.* 2000;42:287.
33. Wei J, Liu J-X, Wu Z-Y, Zhan Z-L, Shi J, Xu K. Research on the electrochemical performance of rutile and anatase composite TiO₂ nanotube arrays in lithium-ion batteries. *J Nanosci Nanotechnol.* 2015;15:5013.
34. Irie H, Watanabe Y, Hashimoto K. Carbon-doped anatase TiO₂ powders as a visible-light sensitive photocatalyst. *Chem Lett.* 2003;32:772-773.
35. Jansen R, Van Bekkum H. XPS of nitrogen-containing functional groups on activated carbon. *Carbon.* 1995;33:1021. Merel M, Tabbal M, Chaker S, Margot MJ. Direct evaluation of the sp³ content in diamond-like-carbon films by XPS. *Appl Surf Sci.* 1998;136:105.
36. Zhang P, Shao C, Zhang Z, et al. TiO₂@carbon core/shell nanofibers: controllable preparation and enhanced visible photocatalytic properties. *Nanoscale.* 2011;3:2943-2949.
37. Mhamane D, Suryawanshi A, Unni SM, Rode C, Kurungot S, Ogale S. Hierarchically nanoporated graphene as a high performance electrode material for ultracapacitors. *Small.* 2013;9: 2801. Ferrari AC, Robertson J. Interpretation of Raman spectra of disordered and amorphous carbon. *Phys Rev B.* 2000;61:14095.
38. Casiraghi C, Pisana S, Novoselov K, Geim A, Ferrari A. Raman fingerprint of charged impurities in graphene. *Appl Phys Lett.* 2007;91:233108.
39. Lv K, Zuo H, Sun J, et al. (Bi, C and N) codoped TiO₂ nanoparticles. *J Hazard Mater.* 2009;161:396. Fang J, Wang F, Qian K, Bao H, Jiang Z, Huang W. Bifunctional N-doped mesoporous TiO₂ photocatalysts. *J Phys Chem C.* 2008;112:18150. Stankovich S, Dikin DA, Piner RD, et al. Synthesis of graphene-based nanosheets via chemical reduction of exfoliated graphite oxide. *Carbon.* 2007;45:1558.
40. Pandolfo A, Hollenkamp A. Carbon properties and their role in supercapacitors. *J Power Sources.* 2006;157:11-27.
41. Banerjee AN, Anitha V, Joo SW. Improved electrochemical properties of morphology-controlled titania/titanate nanostructures prepared by in-situ hydrothermal surface modification of self-source Ti substrate for high-performance supercapacitors. *Sci Rep.* 2017;7:13227.
42. Thommes M, Kaneko K, Neimark AV, et al. Physisorption of gases, with special reference to the evaluation of surface area and pore size distribution (IUPAC technical report). *Pure Appl Chem.* 2015;87:1051-1069.
43. Yu X, Lin D, Li P, Su Z. Recent advances in the synthesis and energy applications of TiO₂-graphene nanohybrids. *Sol Energy Mater Sol Cells.* 2017;172:252-269.
44. Conway BE. *Electrochemical Supercapacitors: Scientific Fundamentals and Technological Applications.* Springer Science & Business Media; 2013;46:855-874.
45. Sundriyal S, Shrivastav V, Sharma M, Mishra S, Deep A. Redox additive electrolyte study of Mn-MOF electrode for supercapacitor applications. *ChemistrySelect.* 2019;4:2585-2592.
46. Wang J, Polleux J, Lim J, Dunn B. Pseudocapacitive contributions to electrochemical energy storage in TiO₂ (Anatase) nanoparticles. *J Phys Chem C.* 2007;111:14925-14931.
47. Augustyn V, Come J, Lowe MA, et al. High-rate electrochemical energy storage through Li⁺ intercalation pseudocapacitance. *Nat Mater.* 2013;12:518. Li H, Lang J, Lei S, et al. A high-performance sodium-ion hybrid capacitor constructed by metal-organic framework-derived anode and cathode materials. *Adv Funct Mater.* 2018;28:1800757.
48. Niu J, Shao R, Liu M, et al. Porous carbon electrodes with battery-capacitive storage features for high performance Li-ion capacitors. *Energy Storage Mater.* 2018;12:145. Xia Q, Yang H, Wang M, et al. High energy and high power lithium-ion capacitors based on boron and nitrogen dual-doped 3D carbon nanofibers as both cathode and anode. *Adv Energy Mater.* 2017;7:1701336.
49. Sundriyal S, Shrivastav V, Sharma M, Mishra S, Deep A. Significantly enhanced performance of rGO/TiO₂ nanosheet composite electrodes based 1.8 V symmetrical supercapacitor with use of redox additive electrolyte. *J Alloys Compd.* 2019; 790:377-387.
50. Lin T-W, Dai C-S, Hung K-C. High energy density asymmetric supercapacitor based on NiOOH/Ni₃S₂/3D graphene and Fe₃O₄/graphene composite electrodes. *Sci Rep.* 2014;4:7274.
51. Sankar KV, Surendran S, Pandi K, et al. Studies on the electrochemical intercalation/de-intercalation mechanism of NiMn₂O₄ for high stable pseudocapacitor electrodes. *RSC Adv.* 2015;5:27649-27656.
52. Singh A, Chandra A. Mining at the Antwerp exposition. *Sci Rep.* 2015;5:15551.
53. Corso BL, Perez I, Sheps T, Sims PC, Gül OT, Collins PG. Electrochemical charge-transfer resistance in carbon nanotube composites. *Nano Lett.* 2014;14:1329. Yang H, Kannappan S., Pandian AS, Jang J-H, Lee YS, Lu W. Preprint arXiv:1311.2013.
54. Ma L, Fan H, Wei X, et al. Towards high areal capacitance, rate capability, and tailorable supercapacitors: Co₃O₄@polypyrrole core-shell nanorod bundle array electrodes. *J Mater Chem A.* 2018;6:19058-19065.
55. Sundriyal S, Mishra S, Deep A. Study of Manganese-1, 4-Benzenedicarboxylate metal organic framework electrodes based solid state symmetrical supercapacitor. *Energy Procedia.* 2019;158:5817-5824.

56. Hu C-C, Tsou T-W. Ideal capacitive behavior of hydrous manganese oxide prepared by anodic deposition. *Electrochem Commun.* 2002;4:105-109.

SUPPORTING INFORMATION

Additional supporting information may be found online in the Supporting Information section at the end of this article.

How to cite this article: Shrivastav V, Sundriyal S, Kim K-H, Sinha RK, Tiwari UK, Deep A. Metal-organic frameworks-derived titanium dioxide-carbon nanocomposite for supercapacitor applications. *Int J Energy Res.* 2020; 44:6269-6284. <https://doi.org/10.1002/er.5328>